Lesion Quantification Accuracy of Digital 90Y PET Imaging in the Context of Dosimetry in Systemic FAPI Radionuclide Therapy

David Kersting[1,2], Walter Jentzen[1,2], Daniel Jeromin[1,2], Ilektra-Antonia Mavroeidi[2,3], Maurizio Conti[4], Florian Büther[5], Ken Herrmann[1,2], Christoph Rischpler[1,2], Rainer Hamacher[2,3], Wolfgang P. Fendler[1,2], Robert Seifert[1,2,5], and Pedro Fragoso Costa[1,2]

[1] Department of Nuclear Medicine, West German Cancer Center (WTZ), University Hospital Essen, University of Duisburg-Essen, Essen, Germany

[2] German Cancer Consortium (DKTK), Partner Site University Hospital Essen, Essen, Germany

[3] Department of Medical Oncology, West German Cancer Center (WTZ), University Hospital Essen, University of Duisburg-Essen, Essen, Germany

[4] Siemens Medical Solutions USA, Inc., Knoxville, TN, United States

[5] Department of Nuclear Medicine, University Hospital Muenster, University of Muenster, Germany

---

Short title: 90Y-FAPI PET Quantification

Corresponding author:

David Kersting, MD M.Sc. (resident-in-training)

ORCID iD: 0000-0002-8451-1830

Department of Nuclear Medicine, University Hospital Essen, University of Duisburg-Essen

Hufelandstrasse 55, D-45147 Essen, Germany

fax: +49-201-723-5964, phone: +49-201-723-2032

email: david.kersting@uni-due.de

ABSTRACT

^{90}Y-FAPI therapy was recently introduced as novel treatment concept for patients with solid tumors. Lesion and organ-at-risk dosimetry is part of assessing treatment efficacy and safety and requires reliable quantification of tissue uptake. As ^{90}Y quantification is limited by the low internal positron-electron pair conversion rate, the increased effective sensitivity, due to improved time-of-flight resolution, of digital silicon photomultiplier-based PET/CT systems might increase quantification accuracy and, consequently, allow for dosimetry in ^{90}Y-FAPI therapy. The aim of this study was to explore the conditions for reliable lesion image quantification in ^{90}Y-FAPI radionuclide therapy using a digital PET/CT system.

Methods: Two tumor phantoms were filled with ^{90}Y solution using different sphere activity concentrations and a constant signal-to-background ratio of 40. The minimum detectable activity concentration was determined and its dependency from acquisition time (15 min vs. 30 min per bed) and smoothing levels (all-pass vs. 5-mm Gaussian filter) was investigated. Quantification accuracy was evaluated at varying activity concentrations to estimate the minimum quantifiable activity concentration based on a contour- and an oversize-based quantification approach. A ±20% deviation range between imaged-derived and true activity concentrations was regarded acceptable. Tumor dosimetry of three ^{90}Y-FAPI therapy patients is presented to project the phantom results to clinical scenarios.

Results: For a lesion size of 40 mm and a clinical acquisition time of 15 min, both minimum detectable and minimum quantifiable activity concentrations were 0.12 MBq/mL. For lesion sizes ≥30 mm, accurate quantification was feasible for detectable lesions. Only for the smallest 10-mm sphere, minimum detectable and minimum quantifiable activity concentration differed substantially (0.43 vs. 1.97 MBq/mL). No notable differences between the two quantification approaches were observed. For the investigated tumors, absorbed dose estimates with a reliable accuracy were achievable.

49   **Conclusions:** For lesion sizes and activity concentrations that are expected to be observed in

50   ^{90}Y-FAPI patients, quantification with reasonable accuracy is possible. Further dosimetry studies are

51   needed to thoroughly investigate efficacy and safety of ^{90}Y-FAPI therapy.

INTRODUCTION

The high-energy beta-particle emitter ^{90}Y is a radionuclide that is used in oncological radionuclide therapy regimens. Typical applications include local radioembolization of hepatocellular carcinoma by selective internal radiation therapy (SIRT) (*1*) or systemic therapies using, for example, somatostatin receptor agonists like ^{90}Y-DOTATATE/DOTATOC to target neuroendocrine tumors after intravenous injection (*2*). Recently, systemic treatments of sarcoma or pancreatic cancer patients using ^{90}Y-labelled fibroblast activation protein inhibitors (FAPIs) were introduced (*3,4*). The target molecule fibroblast activation protein alpha (FAPα) is a cell-surface dipeptidyl peptidase expressed by cancer associated fibroblasts in the tumor microenvironment of various solid tumors as well as cancer cells such as sarcoma and mesothelioma (*5*).

Intra-therapeutic ^{90}Y in imaging in bremsstrahlung whole-body scintigraphy or single-photon emission computed tomography (SPECT) technique are established and well tolerated by patients to rapidly verify tracer accumulation in the tumor tissue and to investigate tracer biodistribution (*6*). However, these imaging modalities do not allow reliable quantification of ^{90}Y activity concentration that is mandatory for intra-therapeutic lesion dosimetry in systemic radionuclide therapy (*7*). Limiting factors are, for example, an inaccurate compensation of scattered and septal penetrating photons of the continuous bremsstrahlung energy spectrum and the difficulty to choose an appropriate energy window, as no discrete gamma photons are emitted (*7,8*). In ^{90}Y-FAPI therapy, lesion dosimetry is required for dose-response investigations and can be part of the decision-making process to apply further therapeutic cycles.

Alternatively to bremsstrahlung imaging, ^{90}Y positron emission tomography (PET) can be performed (*9*) to provide higher visual image quality and a higher detectability for small lesions (*6,8*). Moreover, the possibility of reliable ^{90}Y PET quantification for SIRT was demonstrated (*10*). However, tumor activity concentrations in SIRT are typically high (>1 MBq/mL) (*11*), whereas in systemic radionuclide therapies considerably lower activity concentrations are accumulated by the tumor tissue

77   (*3*). As ^{90}Y PET imaging is limited by poor counting statistics due to internal positron-electron pair

78   conversion occurring in only 0.00326% pairs per decay (*11*), quantification of low activity concentrations

79   is extremely challenging (*12*).

80   The recently introduced "digital" silicon-photomultiplier-based PET/CT systems offer a higher

81   effective sensitivity, spatial, and coincidence timing resolution than previous-generation systems.

82   Therefore, image quality and lesion detectability are improved, particularly for small lesions with low

83   tracer uptake (*13-17*). The improvements were described for different radionuclides (positron branching

84   ratio within parentheses) including ^{18}F (97%) and ^{68}Ga (89%), and the non-standard tracer ^{124}I (23%).

85   Recently, first applications of digital ^{90}Y PET in the context of SIRT were described (*12,18*), but – to the

86   authors' knowledge – no performance evaluation for systemic radionuclide therapy was performed yet.

87   The aim of this study was to explore the conditions for reliable lesion image quantification in ^{90}Y-

88   FAPI radionuclide therapy using a digital PET/CT system.

89

MATERIALS AND METHODS

Study Design

The study consisted of two parts: a phantom and a clinical case study. A National Electrical Manufacturers Association (NEMA) tumor phantom and an anthropomorphic abdominal tumor phantom were scanned under different conditions to estimate the size-dependent minimum detectable activity concentration (MDAC), minimum quantifiable activity concentration (MQAC), and quantification accuracy comparing two approaches for partial-volume effect correction. Additionally, tumor dosimetry of three ^{90}Y-FAPI therapy patients was performed and evaluated, considering the results of the phantom data. Of note, here, a condensed version of the Methods section is shown; full experimental details are presented as Supplemental Data.

Simple Approaches to Correct for Partial-Volume Effect

In clinical tumor dosimetry, the mean imaged activity concentration within the tumor boundary is commonly used to derive the (mean) tumor absorbed (radiation) dose. When using the mean activity concentration, a partial volume effect correction is necessary in any case unless the objects are extremely large, that is, an equivalent sphere diameter of ≥47 times PET spatial resolution ([19]). There are two simple approaches applied in this study to correct for this effect: the contour-based approach uses measured sphere recovery coefficient (RC) values to correct the mean imaged activity concentration within the lesion boundary. RC values were derived from the NEMA tumor phantom. The second approach, the oversize-based approach, includes the total activity within the lesion volume using an oversized volume-of-interest (VOI), whose borders have an approximate distance of one time the PET spatial resolution of the actual geometrical (CT-derived) boundary of the lesion. It is assumed that this oversize VOI contains the main activity to compensate for partial-volume effects; however, to compensate for contribution from background activity a background subtraction was performed as previously described ([20]).

Phantoms

Setup and preparation

The NEMA tumor phantom is a torso-shaped phantom containing 6 spheres (diameters: 9.7, 12.6, 17.4, 22.2, 27.7, and 37.0 mm). The anthropomorphic abdominal tumor phantom (Abdo-Man) (*21*) contains a refillable liver insert, in which 4 spheres (diameters: 10.0, 20.0, 30.0, and 40.0 mm) are attached. It was selected from the phantoms available in our institution to resemble the human body scattering geometry more realistically than the NEMA tumor phantom. Moreover, an investigation of the quantification accuracy on the NEMA phantom would be biased for the contour-based method, as the RC values were determined using images of the same phantom. Based on clinical data, spherical inserts and cavity were filled with ^{90}Y solution at a representative initial sphere activity concentration of about 3.3 MBq/mL and a signal-to-background ratio of about 40. The initial activity concentration was determined as mean of measurements using three different calibrated vial geometries in two different dose calibrators; the maximum error of the initial activity concentration was estimated to be ±7% at the 95% confidence level (Supplemental Table S1). Activity concentrations at PET start time were 3.36, 1.96, 1.22, 0.73, 0.34, 0.20, 0.12, and 0.05 MBq/mL for the NEMA tumor phantom and 3.33, 1.97, 1.23, 0.73, 0.34, 0.20, 0.12, and 0.06 MBq/mL for the anthropomorphic tumor phantom.

PET acquisition and image reconstruction

Phantom PET data were acquired using a single-bed position on a digital Biograph Vision 600 PET/CT scanner (Siemens Healthineers, Erlangen, Germany; detailed specifications in Supplemental Table S2), which exhibits a time-of-flight resolution of 210 ps (*22*). Initially, the NEMA tumor phantom was scanned for 6 h to determine RC values at high counting statistics. Thereafter, PET data of both phantoms were acquired for 30 min and used to reconstruct 30-min and 15-min acquisition time PET images.

137   Images were reconstructed with time-of-flight option and with point-spread-function modelling as

138   previously recommended for quantitative ^{90}Y PET imaging on the Biograph Vision (*12*). Two post-

139   reconstruction smoothing filter levels (all-pass and 5-mm Gaussian filter) were applied. The images had

140   a voxel size of 3.30x3.30x3.00 mm^3 and the measured system spatial resolution (average full width at

141   half maximum) (*23*) was 6.0 mm for a 5-mm Gaussian smoothing filter.

Patients

Patient characteristics

144   Retrospective analysis of clinical data was approved by the local Ethics Committee (permits no.

145   20-9558-BO). Data sets of three patients were included, who suffered from progressive, advanced-stage

146   solitary fibrous tumor (SFT) and received ^{90}Y-FAPI-46 therapy (first cycle) under compassionate access

147   following clinical indication. Radionuclide treatment was decided for in a multidisciplinary tumor board.

148   All patients had either previously shown progressive disease during established treatment options or

149   were not eligible for other established treatment concepts. The administered therapeutic activities were

150   8.90 GBq (patient#1), 3.82 GBq (patient#2), and 3.67 GBq (patient#3).

PET acquisition and image reconstruction

152   PET/CT examinations were scheduled in reference to a previous study (*3*). Because of

153   symptomatic patients and logistical reasons, serial PET/CT acquisition was performed at slightly

154   differing time points: 17, 22, 41 hours p.i. for patient #1, 2, 20, 43 hours p.i. for patient #2, and 1, 4,

155   20 hours p.i. for patient #3. PET data acquisition and image reconstruction was performed as described

156   in the phantom section (acquisition time of 15 min acquisition time per bed and 5-mm Gaussian

157   smoothing filter).

Phantom Analysis

Minimum detectable activity concentration

The images of the NEMA tumor phantom at varying activity concentrations were used to determine the MDAC as previously described ($13,24$). In brief, the visual detectability of each sphere was determined in a human observer study. Next, the signal-to-noise ratio (SNR) of each sphere was determined to estimate the SNR threshold indicating detectability. Finally, the MDAC was calculated for each sphere as the activity concentration at the threshold SNR.

Quantification accuracy evaluation

To evaluate the lesion quantification accuracy, the activity concentration ratio of PET-imaged to (decay corrected) dose calibrator-derived measurements was investigated. A ±20% deviation range of the activity concentration ratio was regarded acceptable considering the uncertainty for the ^{90}Y activity concentration dose calibrator measurement, ^{18}F PET cross-calibration measurement (25), and the frequency of the positron-electron pair conversion ($26-29$).

Minimum quantifiable activity concentration

The results of the quantification accuracy evaluations were used to estimate the MQAC, that is, the minimum activity concentration for that the quantification appears to be reliable. In its derivation, the values of the quantification accuracy should lie within the ±20% deviation range.

Patient Analysis

In the patient analysis, key quantities related to the estimation of the tumor absorbed dose were derived. The procedure has previously been described (3). Briefly, the tumor volumes were estimated by manual segmentation (VOI technique) using the respective CT images and the VOIs were used to determine the tumor uptake values at three imaging time points. Mean tumor activity concentrations were determined using both the contour-based and oversize-based approach. The resulting uptake

181 curves were parameterized by fitting a mono-exponential function to the measured uptake values to

182 determine the effective half-lives. The time-integrated activity coefficients (residence times) were

183 determined and used to estimate the tumor absorbed doses using the sphere model of OLINDA/EXM

184 (*30*). A logarithmic approach was applied for interpolation between tumor absorbed doses in the OLINDA

185 tables.

Software/Statistics

187   PET image analysis and VOI segmentation was performed using PMOD 4.202 (PMOD

188 Technologies, Zurich, Switzerland); MATLAB R2021a (MathWorks, Natick, Massachusetts, USA) was

189 used for data handling and computations. The absorbed tumor dose was calculated using the

190 OLINDA/EXM 2.2 software (Hermes Medical Solutions AB, Stockholm, Sweden). Graphics were created

191 using BioRender.com (BioRender, San Francisco, USA, www.BioRender.com).

192

RESULTS

Recovery Coefficients

Fitting parameters to calculate the RC values, measured, and fitted RC values are listed in Supplemental Table S3. The agreement between fitted and measured RC values was high (maximum percentage deviation of –6%) indicating a small contribution of the fitting process to the total error of the quantification approaches.

Minimum Detectable Activity Concentration

Figure 1 shows exemplary PET images for the NEMA tumor phantom. The human observer study revealed a SNR threshold of ≥6 to distinguish between "not-detected" and "detected" spheres (Supplemental Figure S1). The MDAC for each sphere size is shown in Table 1. The SNR is presented as a function of the activity concentration for all acquisition conditions in Supplemental Figure S2. The 5-mm smoothed images provided an improved detectability for smaller spheres and the MDAC was smaller by a mean factor of 0.54 compared to images without Gaussian smoothing. For a 30-min acquisition time, the MDAC was reduced by a factor of 0.53 compared to the 15-min acquisition time.

As the detectability was higher for the 5-mm Gaussian filter, the following evaluation of the anthropomorphic phantom and patient examples was restricted to this filter size. Moreover, an acquisition time of 30-min per bed position is excessively long and not feasible for pain-stricken patients undergoing ^{90}Y-FAPI-46 therapy (typically, a PET scan comprises at least 2 bed positions); therefore, only an acquisition time of 15-min (per bed position) was further evaluated.

Figure 2 shows exemplary PET maximum intensity projections (MIPs) of the anthropomorphic abdominal tumor phantom. Only detectable spheres were included into the quantification accuracy analysis (defined as activity concentration ≥ size-dependent MDAC using the 9.7-mm, 17.4-mm, 27.7-

215   mm, and 37.0-mm MDAC determined for the NEMA tumor phantom for the 10.0-mm, 20.0-mm, 30.0-

216   mm, and 40.0-mm sphere of the anthropomorphic abdominal tumor phantom, respectively).

217   Quantification accuracy results from the contour- and the oversize-based quantification

218   approaches are shown in Figure 3. For the 40-mm and 30-mm spheres, accurate quantification was

219   feasible for detectable lesions using both approaches. The oversize-based approach revealed slightly

220   more accurate results for the 30-mm sphere. For the 20-mm sphere and activity concentrations

221   ≤1.23 MBq/mL, quantification accuracy for the contour-based method was slightly below the –20%

222   deviation threshold, whereas accurate quantification was feasible down to activity concentrations

223   ≥0.34 MBq/mL using the oversize-based approach. For the smallest (10-mm diameter) sphere,

224   quantification accuracy was limited for activity concentrations ≤1.23 MBq/mL and the contour-based

225   approach revealed slightly more accurate results. In general, a trend towards an underestimation of the

226   activity concentration was observed for low activity concentrations.

Minimum Quantifiable Activity Concentration

228   The MQAC ranged from 0.12 MBq/mL for the 40-mm sphere to 1.97 MBq/mL for the 10-mm

229   sphere. Detailed results are presented in Table 2.

Patient Tumor Dosimetry

231   Exemplarily, lesion dosimetry was performed for three tumor sites in three different patients with

232   thoracic/pleural SFT. In patient #1 an SFT left paracardial supradiaphragmatic, in patient #2 an SFT

233   right lateral of the third thoracic vertebra, and in patient #3 an SFT left lateral of the aortic arch were

234   evaluated (Figures 4–6). Almost all activity concentration measurements were considered reliable

235   (Figure 7). The activity concentration at the last measurement in patient #1 was below the MQAC for

236   the largest sphere investigated in the phantom study (sphere diameter of 40 mm), which is why we did

237   not use the data point for the lesion dosimetry estimation.

238   The relevant key dosimetry data derived from both the oversize- and contour-based

239   quantification approach are listed in Table 3. The tumor absorbed dose estimation ranged from 0.6 to

240   12.0 Gy/GBq. An overall good agreement (absolute percentage deviation < 20%) of the relevant

241   quantities was observed between the two approaches except for the effective half-life of the tumor in

242   patient#1 (8.4 h vs. 12.2 h).

DISCUSSION

FAP-targeted radionuclide therapy is emerging in solid tumor patients and, recently, several case reports and case series have been published using different ligands and radionuclides (*31-33*). For example, ^{90}Y-FAPI therapy was described for treatment of sarcoma and pancreatic cancer patients (*3,4*) as well as a patient with both breast and colorectal cancer (*34*). Safety and efficacy studies, including dosimetry, have been reported for ^{177}Lu-labelled FAP–targeted radionuclide therapy (*32,35*). Given that ^{90}Y-based dosimetry for systemic radioligand therapy is not as well established and documented as for ^{177}Lu, it is even more important to establish the basis for accurate radionuclide quantification. This will have relevance in pharmacovigilance processes of authorization, such as the evaluation of safety, in the form of dosimetry for organs at risk, and efficacy, in the form of tumor dosimetry to investigate the dose-effects of novel ^{90}Y radioligand therapy agents.

In this study, we applied a heuristic approach for reliable lesion quantification in ^{90}Y-FAPI therapy. To the best of our knowledge, no reports on reliable PET-derived ^{90}Y tumor quantification for activity concentration ranges as they appear in systemic radionuclide therapies have yet been published. The phantom evaluation (Figures 1 and 2) showed that for detectable lesions ≥30 mm in diameter a reliable quantification is feasible (Figure 3). For the 20-mm diameter sphere, the difference between MQAC and MDAC was low (0.34 MBq/mL vs. 0.16 MBq/mL). Only for the smallest sphere (10-mm diameter), the MQAC was notably higher than the MDAC (1.97 MBq/mL vs. 0.43 MBq/mL). Possible explanations are the low absolute amount of ^{90}Y activity resulting in poor counting statistics and the proximity to the 40-mm sphere (also see a comparison of MDAC between NEMA and anthropomorphic phantoms in Supplemental Material and Supplemental Table 4).

In current clinical scenarios, patients undergoing ^{90}Y-FAPI-46 therapy will most likely exhibit larger tumor masses, as this therapy is offered in end-stage diseases when established therapy options have already been exhausted (*3,4*). In the evaluated patient cases (Figures 4-7), the accumulated tumor activity concentration was, except for one data point, larger than the size-dependent MQAC of

268   0.12 MBq/mL (40-mm diameter lesion). We therefore assume that reliable quantification in the context

269   of intra-therapeutic tumor dosimetry is feasible in ^{90}Y-FAPI-46 therapy using a digital PET/CT system.

270   Tumor absorbed dose estimation ranged from 0.6 to 12.0 Gy/GBq (Table 3).

271   As cancer-associated fibroblasts (CAFs) were described to be non-uniformly distributed in the

272   tumor microenvironment (*36*), ^{90}Y-FAPI accumulation will most likely follow that pattern and lead to non-

273   uniform tumor uptake in PET imaging. Due to the high beta particle energy of ^{90}Y leading to a high

274   particle range, tumor cells surrounding the FAP-expressing CAFs will be target to crossfire and

275   bystander radiation (*37*). Therefore, ^{90}Y that deposits its energy in up to 1 cm distance may be more

276   suitable for FAPI radionuclide therapy than ^{177}Lu with an energy deposition in close vicinity of the source

277   (*38*). However, the consequences of non-uniform FAPI uptake on quantification of accumulated activity,

278   dosimetry, and dose response remain yet unclear. In our study, quantification approaches were

279   projected without adjustments from the homogeneous conditions of the phantom study to the patient

280   images. Therefore, accumulated activity was measured as mean activity concentration. This might be

281   an appropriate approach when assuming a high influence of crossfire and bystander effects, which may

282   lead to a homogenization of the radiation dose. Voxel-based dosimetry might be an alternative to take

283   into account non-uniform activity distribution (*39*); however, its clinical relevance may be limited by the

284   low accumulated activity concentrations in systemic ^{90}Y radionuclide therapy.

285   Future evaluations of clinical data will be necessary to investigate possible effects on determined

286   tumor dose and especially dose-response effects to select the optimal quantification approach. With

287   increasing application of ^{90}Y FAPI therapy sufficient data will probably be available for a systematic

288   evaluation. At the moment, the number of investigated patients with sufficient follow-up data is limited.

289   Here, we investigate the quantification accuracy of a current-generation PET scanner as a basis for

290   future clinical evaluations.

291   The comparison between 15-min and 30-min acquisition time per bed position revealed a lower

292   MDAC for the 30-min acquisition time by a factor of approximately two (Table 1). Thus, an approximate

293   linear correlation between MDAC and acquisition time was observed. This finding is in line with the

294   results of a previous study using a different radionuclide *(13)*. Typically, PET scans in ^{90}Y-based therapy

295   patients are performed using at least 2 bed positions (*3*). Therefore, in most patients an extension of the

296   acquisition time will most likely not be tolerable. Moreover, detectability was improved, if a 5-mm

297   Gaussian filter was applied (Table 1). In a systematic comparison of previous generation Siemens

298   PET/CT systems for quantitative ^{90}Y imaging, the usage of a Gaussian filter was left to the user's

299   decision (*40*). We therefore propose an acquisition time of 15 min for clinical imaging protocols and the

300   application of a 5-mm Gaussian filter.

301   Both evaluated quantification methods exhibit limitations and opportunities. On one hand, the

302   contour-based approach is more reproducible, but it has no background activity concentration

303   correction. On the other hand, while it is certain that the oversize-based approach will represent the

304   lesion activity surrounded by a uniform and low activity concentration background, it may be challenging

305   to account for non-uniform background, making the quantification prone to error. Regarding

306   quantification accuracy in phantom data and estimated activity concentrations in patient data, both

307   methods yielded comparable results (Figure 3 and Figure 7), probably due to a low and visually uniform

308   background. Larger differences might be possible for tumor lesions close to a region with high

309   physiological tracer accumulation like the kidney.

310   Only few previous studies were published to investigate ^{90}Y PET imaging in the context of

311   systemic radionuclide therapy and none of these used a digital PET system. Fabbri *et al.* (*41*) identified

312   a MDAC of 0.20 MBq/mL for the three largest spheres of the NEMA tumor phantom using a previous-

313   generation time-of-flight-capable PET scanner. In that study, 30-min acquisitions with zero background

314   activity were reconstructed with 3D ordered-subset expectation maximization using 2 iterations and 4

315   subsets and a 5-mm Gaussian filter. In our study, for a 30-min acquisition time the MDAC was smaller

316   (0.06-0.09 MBq/mL, Table 1). The improvement is explained by the improved time-of-flight resolution of

317   the digital PET system and comparable to the improvement that we observed in a direct comparison

318   between two PET/CT systems for [124]I (*13*). Of note, the study by Fabbri *et al.* (*41*) did not investigate the

319   quantification accuracy. Walrand *et al.* also investigated previous-generation PET systems (*42*) and

320 predicted a reliable estimation of the mean absorbed kidney dose after ^{90}Y-DOTATOC therapy using a

321 kidney phantom filled with an activity concentration of about 0.33 MBq/mL that is substantially larger

322 than the MQAC for the largest sphere in our study (0.12 MBq/mL). Moreover, the investigated kidney

323 cortex had a volume of 107 mL that is considerably larger than the largest sphere in our study (sphere

324 volume 33.5 mL).

325   Future improvements might be possible by application of total body PET/CT scanners (*43*) that

326 cover an extended field-of-view and allow complete acquisition of all necessary PET data in a patient

327 scan using a single bed position. Moreover, an increased sensitivity may allow for shorter acquisition

328 times (*44*) or, alternatively, improved detection and quantification accuracy of lesions at lower activity

329 concentrations.

330 **CONCLUSION**

331   For ^{90}Y$^-$lesions of ≥40-mm diameter, as they typically appear in FAPI radionuclide therapy

332 patients, reliable quantification was possible for activity concentrations of at least 0.12 MBq/mL using a

333 digital PET system. For lesions of ≥30-mm diameter, minimum detectable activity and minimum

334 quantifiable activity were in good agreement, suggesting that dosimetry can be performed for detectable

335 lesions. Further dosimetry studies are needed to thoroughly investigate efficacy and safety of novel ^{90}Y-

336 FAPI based radionuclide therapies.

DISCLOSURE

ACKNOWLEDGMENT

KEY POINTS

QUESTION: Does digital PET allow reliable quantification for lesion dosimetry in ^{90}Y-FAPI radionuclide therapy?

PERTINENT FINDINGS: For lesion sizes and activity concentrations that are expected to be observed in ^{90}Y-FAPI patients, quantification with reasonable accuracy is possible.

IMPLICATIONS FOR PATIENT CARE: Reliable lesion dosimetry in ^{90}Y-FAPI radionuclide therapy is mandatory for dose-response evaluations and for decision of treatment continuation.

REFERENCES

1.   Dancey JE, Shepherd FA, Paul K, et al. Treatment of nonresectable hepatocellular carcinoma with intrahepatic 90Y-microspheres. *J Nucl Med.* 2000;41:1673-1681.

2.   Strosberg J, El-Haddad G, Wolin E, et al. Phase 3 Trial of (177)Lu-Dotatate for midgut neuroendocrine tumors. *N Engl J Med.* 2017;376:125-135.

3.   Ferdinandus J, Costa PF, Kessler L, et al. Initial clinical experience with (90)Y-FAPI-46 radioligand therapy for advanced-stage solid tumors: a case series of 9 patients. *J Nucl Med.* 2022;63:727-734.

4.   Fendler WP, Pabst KM, Kessler L, et al. Safety and efficacy of 90Y-FAPI-46 radioligand therapy in patients with advanced sarcoma and other cancer entities. *Clin Cancer Res.* 2022;Epub ahead of print.

5.   Liu F, Qi L, Liu B, et al. Fibroblast activation protein overexpression and clinical implications in solid tumors: a meta-analysis. *PLoS One.* 2015;10:e0116683.

6.   Brosch J, Gosewisch A, Kaiser L, et al. 3D image-based dosimetry for Yttrium-90 radioembolization of hepatocellular carcinoma: Impact of imaging method on absorbed dose estimates. *Phys Med.* 2020;80:317-326.

7.   Elschot M, Vermolen BJ, Lam MG, de Keizer B, van den Bosch MA, de Jong HW. Quantitative comparison of PET and Bremsstrahlung SPECT for imaging the in vivo yttrium-90 microsphere distribution after liver radioembolization. *PloS one.* 2013;8:e55742.

8.   Kubik A, Budzynska A, Kacperski K, et al. Evaluation of qualitative and quantitative data of Y-90 imaging in SPECT/CT and PET/CT phantom studies. *PLoS One.* 2021;16:e0246848.

9.   Wright CL, Zhang J, Tweedle MF, Knopp MV, Hall NC. Theranostic Imaging of Yttrium-90. *Biomed Res Int.* 2015;2015:481279.

390   **10.**   Lhommel R, van Elmbt L, Goffette P, et al. Feasibility of 90Y TOF PET-based dosimetry in liver

391   metastasis therapy using SIR-Spheres. *Eur J Nucl Med Mol Imaging.* 2010;37:1654-1662.

392   **11.**   Pasciak AS, Bourgeois AC, McKinney JM, et al. Radioembolization and the dynamic role of (90)Y

393   PET/CT. *Front Oncol.* 2014;4:38.

394   **12.**   Kunnen B, Beijst C, Lam M, Viergever MA, de Jong H. Comparison of the Biograph Vision and

395   Biograph mCT for quantitative (90)Y PET/CT imaging for radioembolisation. *EJNMMI Phys.* 2020;7:14.

396   **13.**   Kersting D, Jentzen W, Fragoso Costa P, et al. Silicon-photomultiplier-based PET/CT reduces

397   the minimum detectable activity of iodine-124. *Sci Rep.* 2021;11:17477.

398   **14.**   Weber M, Jentzen W, Hofferber R, et al. Evaluation of [(68)Ga]Ga-PSMA PET/CT images

399   acquired with a reduced scan time duration in prostate cancer patients using the digital biograph vision.

400   *EJNMMI Res.* 2021;11:21.

401   **15.**   Weber M, Jentzen W, Hofferber R, et al. Evaluation of (18)F-FDG PET/CT images acquired with

402   a reduced scan time duration in lymphoma patients using the digital biograph vision. *BMC Cancer.*

403   2021;21:62.

404   **16.**   Fragoso Costa P, Jentzen W, F SU, et al. Reduction of emission time for [68Ga]Ga-PSMA

405   PET/CT using the digital biograph vision: a phantom study. *Q J Nucl Med Mol Imaging.* 2021;Epub

406   ahead of print.

407   **17.**   Kersting D, Jentzen W, Sraieb M, et al. Comparing lesion detection efficacy and image quality

408   across different PET system generations to optimize the iodine-124 PET protocol for recurrent thyroid

409   cancer. *EJNMMI Phys.* 2021;8:14.

410   **18.**   Labour J, Boissard P, Baudier T, et al. Yttrium-90 quantitative phantom study using digital photon

411   counting PET. *EJNMMI Phys.* 2021;8:56.

412   **19.**   Jentzen W. Experimental investigation of factors affecting the absolute recovery coefficients in

413   iodine-124 PET lesion imaging. *Phys Med Biol.* 2010;55:2365-2398.

414   **20.**   Walrand S, Jamar F, Mathieu I, et al. Quantitation in PET using isotopes emitting prompt single

415   gammas: application to yttrium-86. *Eur J Nucl Med Mol Imaging.* 2003;30:354-361.

416   **21.**   Gear JI, Cummings C, Craig AJ, et al. Abdo-Man: a 3D-printed anthropomorphic phantom for

417   validating quantitative SIRT. *EJNMMI physics.* 2016;3:1-16.

418   **22.**   van Sluis J, de Jong J, Schaar J, et al. Performance characteristics of the digital Biograph Vision

419   PET/CT system. *J Nucl Med.* 2019;60:1031-1036.

420   **23.**   Jentzen W, Weise R, Kupferschlager J, et al. Iodine-124 PET dosimetry in differentiated thyroid

421   cancer: recovery coefficient in 2D and 3D modes for PET(/CT) systems. *Eur J Nucl Med Mol Imaging.*

422   2008;35:611-623.

423   **24.**   Oen SK, Aasheim LB, Eikenes L, Karlberg AM. Image quality and detectability in Siemens

424   Biograph PET/MRI and PET/CT systems-a phantom study. *EJNMMI Phys.* 2019;6:16.

425   **25.**   Keller SH, Jakoby B, Svalling S, Kjaer A, Hojgaard L, Klausen TL. Cross-calibration of the

426   Siemens mMR: easily acquired accurate PET phantom measurements, long-term stability and

427   reproducibility. *EJNMMI Phys.* 2016;3:11.

428   **26.**   Dryak P, Solc J. Measurement of the branching ratio related to the internal pair production of Y-

429   90. *Appl Radiat Isot.* 2020;156:108942.

430   **27.**   Chistsé V, Bé MM. 90Y – comments on evaluation of decay data. Decay Data Evaluation Project

431   website.   http://www.nucleide.org/DDEP_WG/Nuclides/Y-90_com.pdf.   Updated   November   2016.

432   Accessed 03 March 2022.; 2015.

433   **28.**   Staníček J. Emission of positrons in beta-decay of 90Sr + 90Y. *Acta Phys Univ Comen.* 2007:51-

434   56.

435 **29.** Selwyn RG, Nickles RJ, Thomadsen BR, DeWerd LA, Micka JA. A new internal pair production

436 branching ratio of 90Y: the development of a non-destructive assay for 90Y and 90Sr. *Appl Radiat Isot.*

437 2007;65:318-327.

438 **30.** Stabin MG, Sparks RB, Crowe E. OLINDA/EXM: the second-generation personal computer

439 software for internal dose assessment in nuclear medicine. *J Nucl Med.* 2005;46:1023-1027.

440 **31.** Assadi M, Rekabpour SJ, Jafari E, et al. Feasibility and therapeutic potential of 177Lu-Fibroblast

441 Activation Protein Inhibitor-46 for patients with relapsed or refractory cancers: a preliminary study. *Clin*

442 *Nucl Med.* 2021;46:e523-e530.

443 **32.** Ballal S, Yadav MP, Moon ES, et al. First-in-human results on the biodistribution,

444 pharmacokinetics, and dosimetry of [(177)Lu]Lu-DOTA.SA.FAPi and [(177)Lu]Lu-DOTAGA.(SA.FAPi)2.

445 *Pharmaceuticals (Basel).* 2021;14.

446 **33.** Fu K, Pang Y, Zhao L, et al. FAP-targeted radionuclide therapy with [(177)Lu]Lu-FAPI-46 in

447 metastatic nasopharyngeal carcinoma. *Eur J Nucl Med Mol Imaging.* 2022;49:1767-1769.

448 **34.** Rathke H, Fuxius S, Giesel FL, et al. Two tumors, one target: preliminary experience with 90Y-

449 FAPI therapy in a patient with metastasized breast and colorectal cancer. *Clin Nucl Med.* 2021;46:842-

450 844.

451 **35.** Kuyumcu S, Kovan B, Sanli Y, et al. Safety of ibroblast Activation Protein-targeted radionuclide

452 therapy by a low-dose dosimetric approach using 177Lu-FAPI04. *Clin Nucl Med.* 2021;46:641-646.

453 **36.** Sahai E, Astsaturov I, Cukierman E, et al. A framework for advancing our understanding of

454 cancer-associated fibroblasts. *Nat Rev Cancer.* 2020;20:174-186.

455 **37.** Freudenberg R, Wendisch M, Kotzerke J. Geant4-Simulations for cellular dosimetry in nuclear

456 medicine. *Z Med Phys.* 2011;21:281-289.

457   **38.**   Brady D, O'Sullivan JM, Prise KM. What is the role of the bystander response in radionuclide

458   therapies? *Front Oncol.* 2013;3:215.

459   **39.**   Chiesa C, Bardies M, Zaidi H. Voxel-based dosimetry is superior to mean absorbed dose

460   approach for establishing dose-effect relationship in targeted radionuclide therapy. *Med Phys.*

461   2019;46:5403-5406.

462   **40.**   Willowson KP, Tapner M, Team QI, Bailey DL. A multicentre comparison of quantitative (90)Y

463   PET/CT for dosimetric purposes after radioembolization with resin microspheres : The QUEST Phantom

464   Study. *Eur J Nucl Med Mol Imaging.* 2015;42:1202-1222.

465   **41.**   Fabbri C, Bartolomei M, Mattone V, et al. 90Y-PET/CT imaging quantification for dosimetry in

466   peptide receptor radionuclide therapy: Analysis and corrections of the impairing factors. *Cancer*

467   *Biotherapy and Radiopharmaceuticals.* 2015;30:200-210.

468   **42.**   Walrand S, Jamar F, van Elmbt L, Lhommel R, Bekonde EBa, Pauwels S. 4-Step renal dosimetry

469   dependent on cortex geometry applied to 90Y peptide receptor radiotherapy: evaluation using a fillable

470   kidney phantom imaged by 90Y PET. *Journal of Nuclear Medicine.* 2010;51:1969-1973.

471   **43.**   Zhang YQ, Hu PC, Wu RZ, et al. The image quality, lesion detectability, and acquisition time of

472   (18)F-FDG total-body PET/CT in oncological patients. *Eur J Nucl Med Mol Imaging.* 2020;47:2507-2515.

473   **44.**   Alberts I, Hunermund JN, Prenosil G, et al. Clinical performance of long axial field of view

474   PET/CT: a head-to-head intra-individual comparison of the Biograph Vision Quadra with the Biograph

475   Vision PET/CT. *Eur J Nucl Med Mol Imaging.* 2021;48:2395-2404.

FIGURES
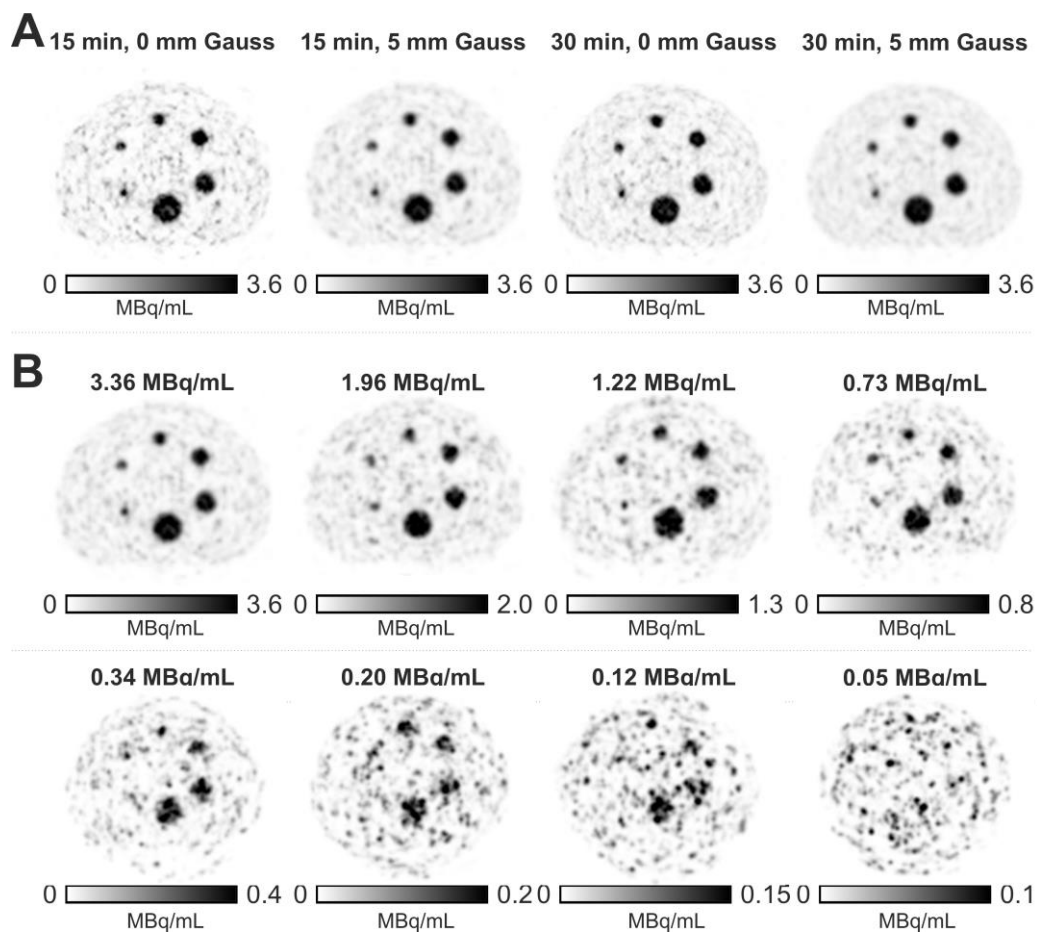
Figure 1: PET images of the NEMA tumor phantom

Figure 1. NEMA tumor phantom images showing (A) the different investigated emission times and Gaussian filter levels at the highest sphere activity concentration of 3.36 MBq/mL and (B) the different investigated sphere activity concentrations for a 15-min acquisition time and 5-mm Gaussian smoothing level.

479   **Figure 2: PET MIP of the anthropomorphic abdominal tumor phantom**
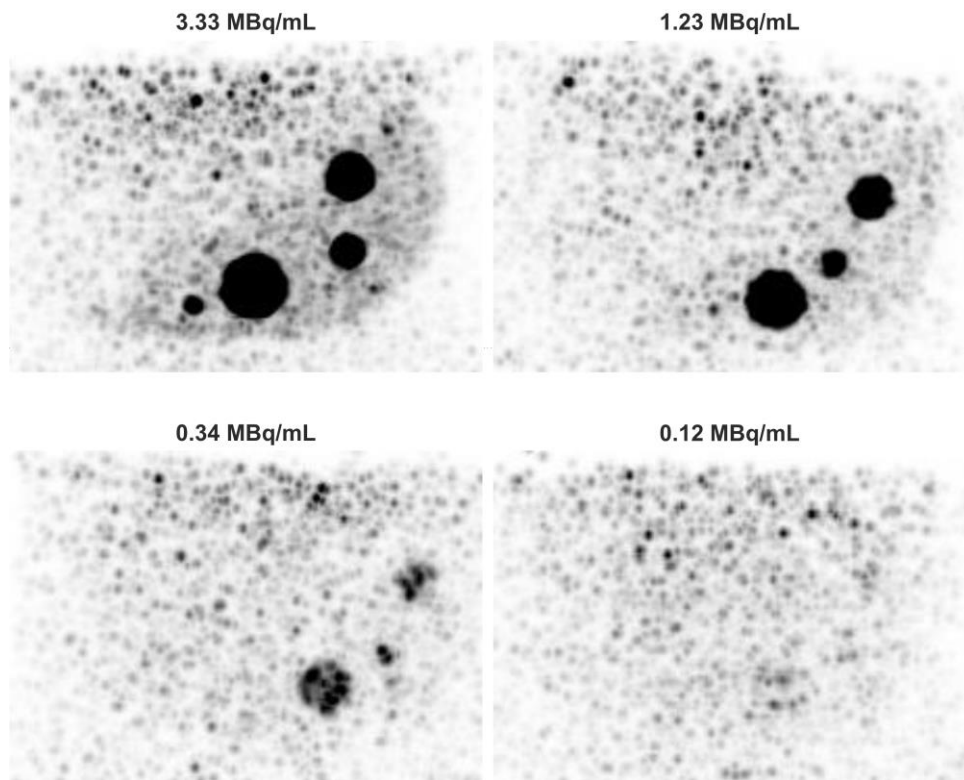

Figure 2. PET MIP of the anthropomorphic abdominal tumor phantom images at four different activity concentration levels. Images were reconstructed using 15-min acquisition data and smoothed with a 5-mm Gaussian filter.

480

Figure 3: Quantification accuracy using the anthropomorphic tumor phantom
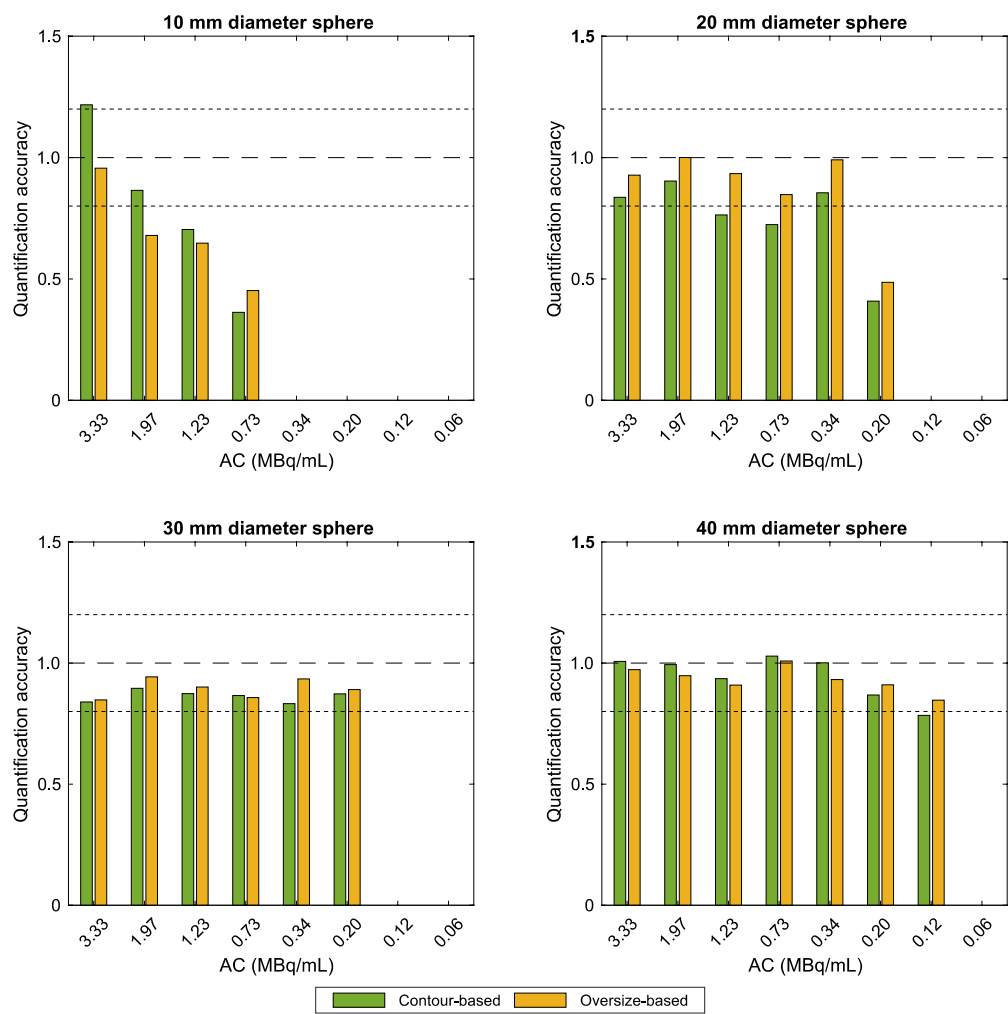
Figure 3. Contour- and oversize-based quantification accuracy using the anthropomorphic tumor phantom. Dashed horizontal line indicate ±20 % error margins. Missing bars correspond to spheres regarded as "not-detected" and as such not considered for quantification accuracy evaluation. PET images with 5-mm Gaussian filter and an acquisition time of 15 minutes (per bed position) were analyzed only.

482

Figure 4: Patient 1 – PET/CT imaging and lesion delineation

Figure 4. 90Y-FAPI-46 PET MIP of patient #1 (A) with axial PET/CT images (B) displaying the contour-based VOI (blue) and oversize-based VOI (green). Only the two first PET data on panel A were considered for tumor absorbed dose estimation.

Figure 5: Patient 2 – PET/CT imaging and lesion delineation
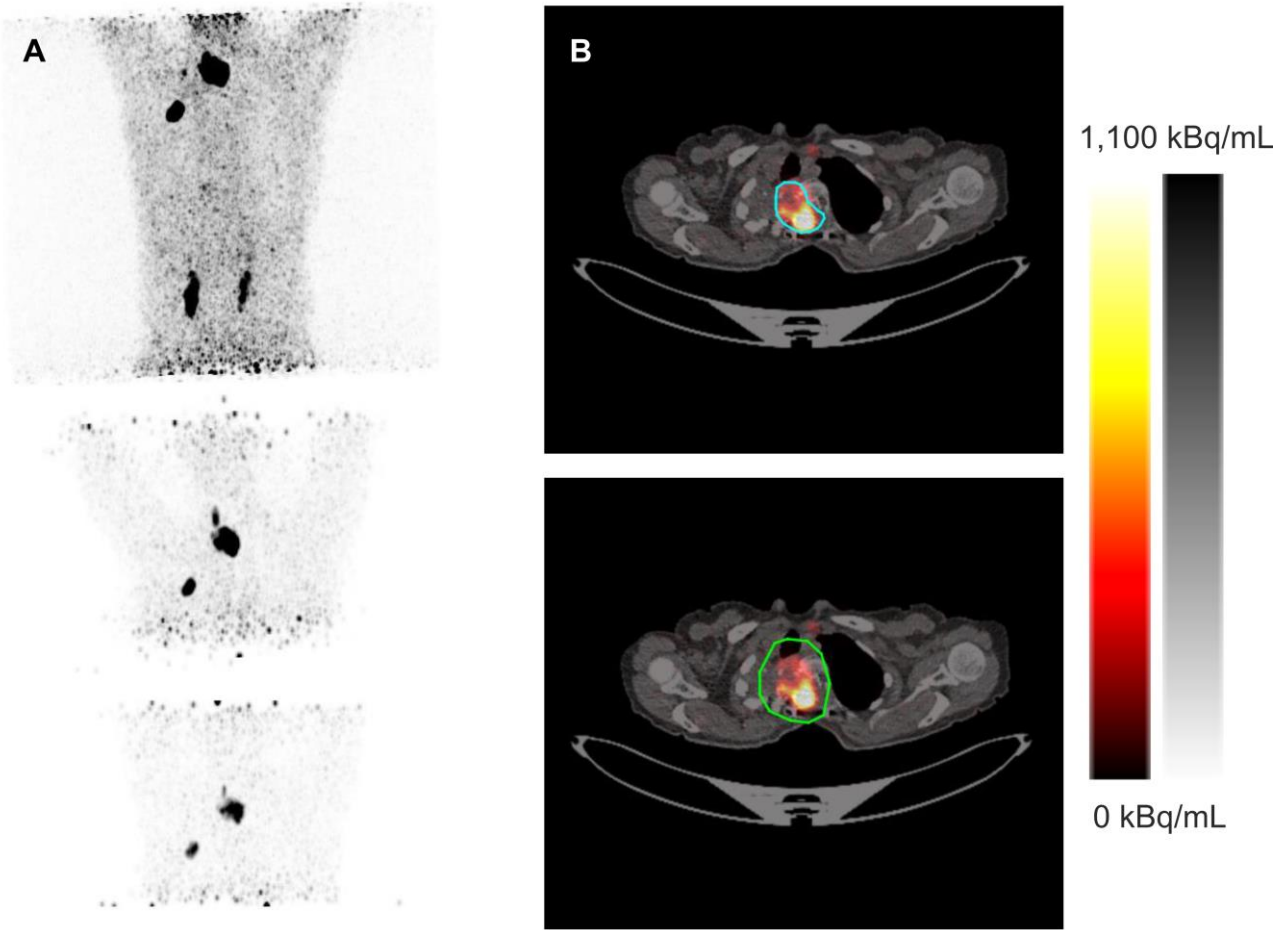
Figure 5. ⁹⁰Y-FAPI-46 PET MIP of patient #2 (A) with axial PET/CT images (B) displaying the contour-based VOI (blue) and oversize-based VOI (green).

486

Figure 6: Patient 3 – PET/CT imaging and lesion delineation
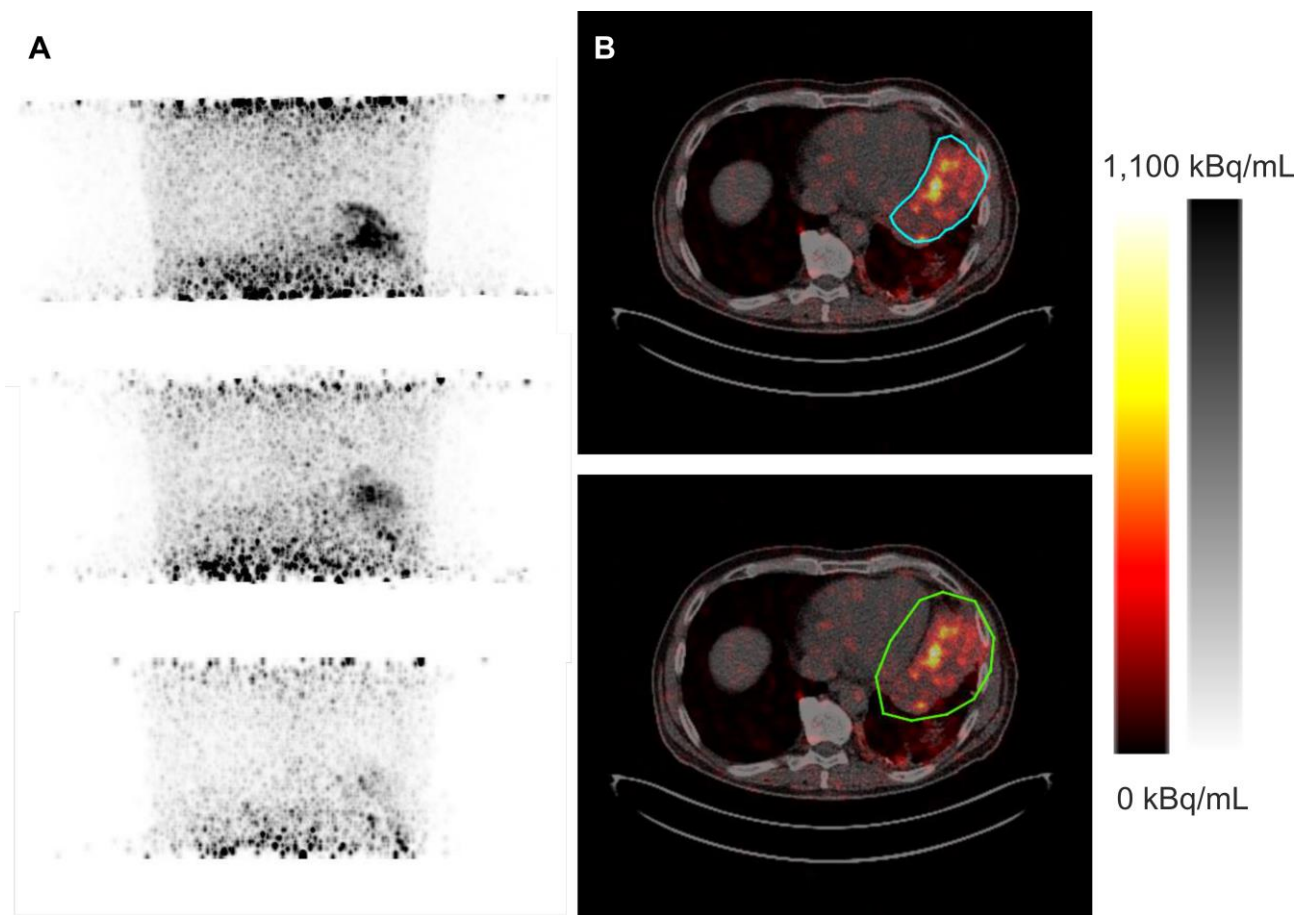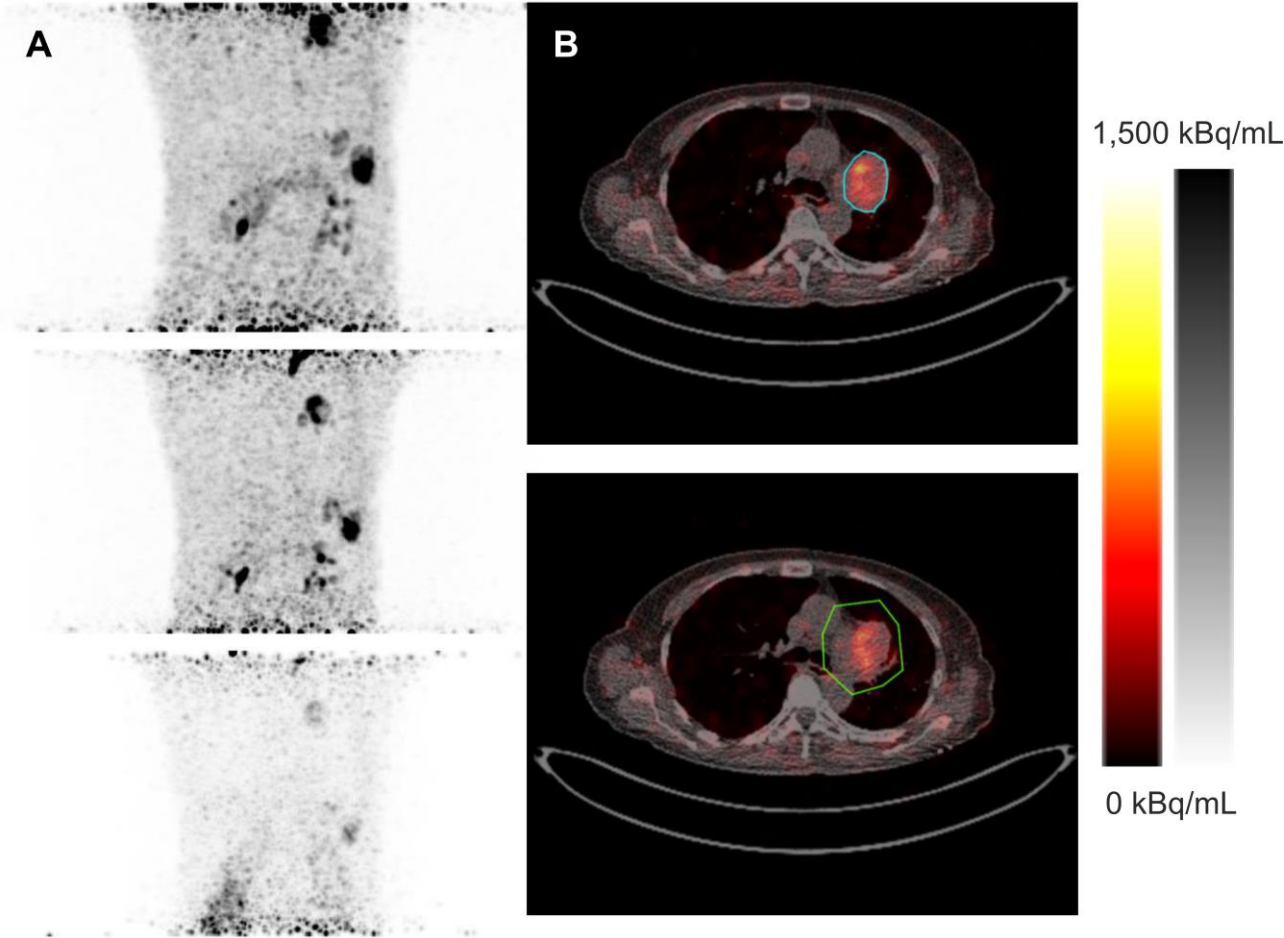

Figure 6. ^{90}Y-FAPI-46 PET MIP of patient #3 (A) with axial PET/CT images (B) displaying the contour-based VOI (blue) and oversize-based VOI (green).

488

Figure 7: Tumor activity concentrations at three time points
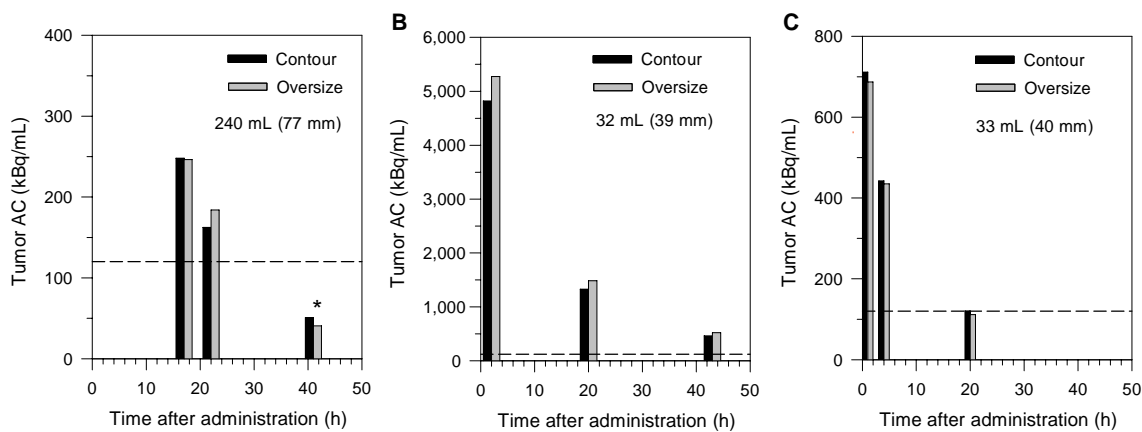
Figure 7. Tumor activity concentration derived from either the contour-based or oversize-based approach as a function of time after administration. Values within parenthesizes are the respective sphere-equivalent diameters. Activity concentrations above the dashed lines indicate reliable quantification based on Figure 3. A value that appears to be "unreliable" in terms of quantification is marked with an asterisk (details in main body of the text).

490

491 # TABLES

492 **Table 1: Minimum detectable activity concentration**

Table 1. Estimated minimum detectable activity concentration (in MBq/mL) for the investigated sphere diameters, acquisition time durations (15 min vs. 30 min), and smoothing levels (all-pass vs. 5-mm Gaussian filter).

Diameter	All-pass		5-mm smoothing	
(mm)	15 min	30 min	15 min	30 min
9.7	0.71	0.44	0.43	0.33
12.6	0.51	0.23	0.30	0.17
17.4	0.37	0.15	0.16	0.07
22.2	0.37	0.18	0.18	0.09
27.7	0.29	0.16	0.15	0.08
37.0	0.27	0.14	0.12	0.06

493

494 **Table 2: Minimum quantifiable activity concentration**

Table 2. Estimated minimum quantifiable activity concentration (MQAC) of reliability at different lesion sizes derived from images reconstructed with 15-min acquisition time data and smoothed with a 5-mm Gaussian filter.

Diameter (mm)	10	20	30	40
MQAC (MBq/mL)	1.97	0.34	0.20	0.12

495

496

Table 3: Key tumor dosimetry quantities

Table 3. Key dosimetry quantities – tumor volume (V) and its respective sphere equivalent diameter (d), time-integrated activity coefficient (TIAC), effective half-life (T_{eff}) – to estimate the tumor absorbed dose per administered activity (AD) using the contour- and oversize-based approaches.

		Contour-based			Oversize-based		
Patient #	V / d	TIAC	T_{eff}	AD	TIAC	T_{eff}	AD
	(mL/mm)	(min)	(h)	(Gy/GBq)	(min)	(h)	(Gy/GBq)
1	240 (77)	17	8.4	0.62	17	12.2	0.60
2	32 (39)	42	12.3	10.90	47	12.4	12.00
3	33 (40)	4	7.5	0.98	4	7.3	0.93

498
499
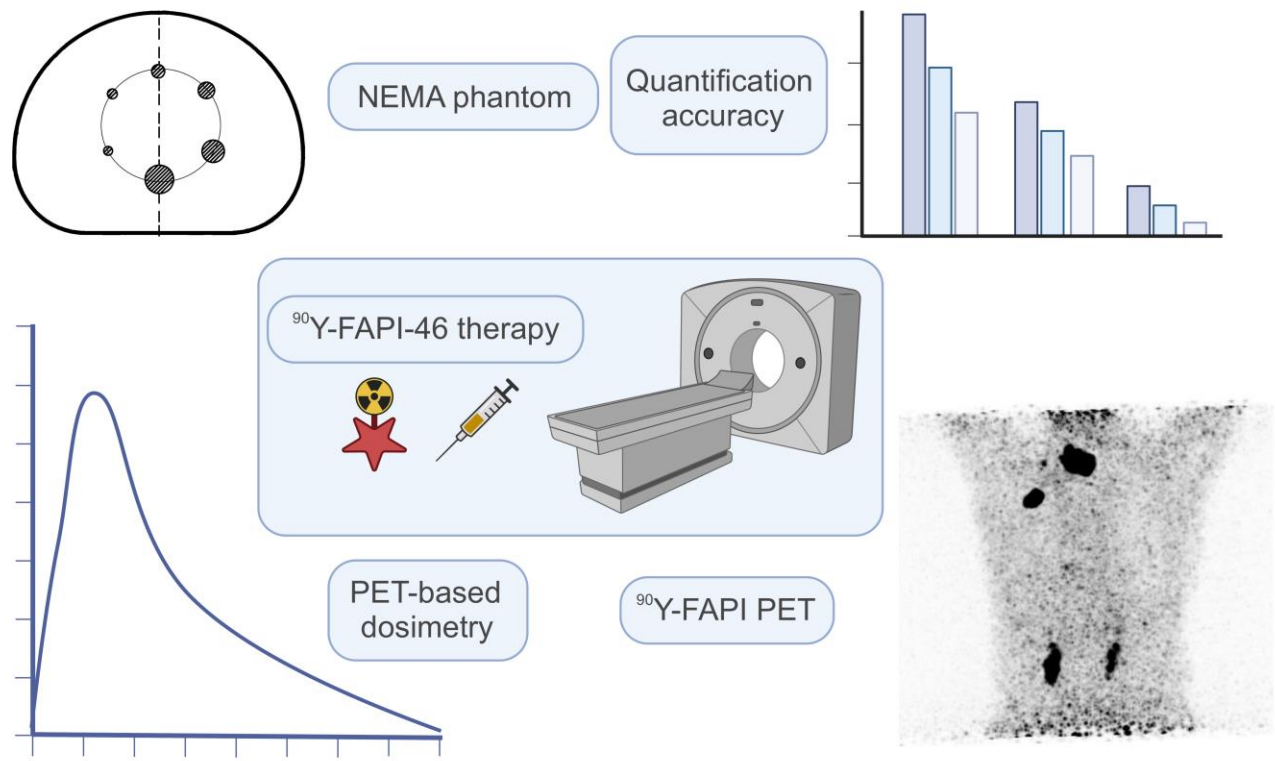
GRAPHICAL ABSTRACT

NEMA phantom

Quantification accuracy

^{90}Y-FAPI-46 therapy

PET-based dosimetry

^{90}Y-FAPI PET

"Lesion Quantification Accuracy of Digital ^{90}Y PET Imaging in the Context of Dosimetry in Systemic FAPI Radionuclide Therapy"

Simple Approaches to Correct for Partial-Volume Effect

In the following, the term lesion refers to both the spherical inserts of the tumor phantoms or the tumor within the patient. Of note, in clinical tumor dosimetry, the mean imaged activity concentration within the tumor boundary is commonly used to derive the (mean) tumor absorbed (radiation) dose. When using the mean activity concentration, a partial volume effect correction is necessary in any case unless the objects are extremely large, that is, an equivalent sphere diameter of ≥47 times PET spatial resolution (*19*). There are two simple approaches applied in this study to correct for this effect: a contour- and an oversize-based approach.

Contour-based approach. The contour-based approach uses sphere recovery coefficient (RC) values to correct the mean imaged activity concentration within the lesion boundary, that is, the mean imaged activity concentration (C_{imaged}) was divided by the diameter-dependent RC value and termed contour-based corrected activity concentration. The sphere RC values were derived from the NEMA tumor phantom images.

$$C_{corrected} = \frac{C_{imaged}}{RC(d)}$$

It is $C_{corrected}$ the contour-corrected activity concentration. In the application, the tumor geometry is assumed to be a volume-equivalent sphere with an effective diameter d.

1 / 15

Oversize-based approach. For the oversize-based approach, the total activity ($A_{oversize}$) within the lesion volume (V_{lesion}) is determined using an oversized VOI ($V_{oversize}$), that is, the points of the oversize VOI have an approximate distance of one time the PET spatial resolution of the actual geometrical boundary of the lesion. It is assumed that this oversize VOI (with its volume $V_{oversize}$) contained the main activity to compensate for partial-volume effects; however, the oversize VOI contains contribution from a background activity and requires a correction. The background subtraction can be conducted as follows ([20]):

$$C_{corrected} = \frac{A_{oversize} - \left(V_{oversize} - V_{lesion}\right) \cdot C_{bgr}}{V_{lesion}}$$

It is $C_{corrected}$ and C_{bgr} the oversize-corrected and background activity concentration, respectively. The background activity concentration is the local background derived from a representative background VOI close to the lesion. Of note, this approach assumes a uniform background activity concentration.

Activity Measurements

Three independent vial geometries – 10-mL TEMA syringe, 10-mL Becton & Dickinson syringe (B&D), 11-mL TechneVial – were used to measure the ^{90}Y activity in two different dose calibrators (CRC-25R and CRC-15R, Capintec Inc., Ramsey, NJ, USA). Each vial geometry was calibrated by a metrology institution. The mean of these activity concentration measurements along with their 95% confidence level was calculated and used to determine the reference activity concentration and its maximum error. The reference activity concentration and error estimate was 3.58 MBq/mL ±7% at the 95%-confidence level (Supplemental Table S1).

PET/CT System

The digital PET/CT system used for phantom and patient examinations was a Biograph Vision 600 PET/CT scanner (Siemens Healthineers, Erlangen, Germany). Detailed scanner

specifications were published elsewhere (*22*) and are summarized in Supplemental Table S2. For this system, the branching ratio related to the internal pair production of ^{90}Y and the ^{90}Y half-life were 0.0032% and 64.053 h, respectively.

Phantoms

Setup and preparation

Tumor phantoms. Two types of tumor phantoms were used. First, the NEMA tumor phantom (NEMA IEC/2001 body phantom) is a torso-shaped phantom (torso volume of 9720 mL) containing 6 spheres (diameters: 9.7, 12.6, 17.4, 22.2, 27.7, and 37.0 mm) to simulate hot lesions in a uniform warm background. Second, the anthropomorphic abdominal tumor phantom (Abdo-Man) was originally designed for quantitative imaging analysis of selective internal radiation therapy (*21*). The phantom contains a refillable liver insert (inner volume of 1768 mL), in which 4 spheres (diameters: 10.0, 20.0, 30.0, and 40.0 mm) are attached. It was selected from the phantoms available in our institution to resemble the human body scattering geometry more realistically than the NEMA tumor phantom.

Preparation. Based on clinical data, the spherical inserts and the cavity were filled with ^{90}Y in aqueous solution at a representative initial sphere activity concentration of about 3.3 MBq/mL and a signal-to-background ratio of about 40 at PET start time. To prevent binding of ^{90}Y to the phantom and sphere walls, the chelator DTPA was added in excess to the ^{90}Y solution; acetate buffer was used to adjust a pH value of about 6.5. PET imaging was performed directly following preparation and at 7 additional time points spaced approximately one ^{90}Y half-life apart to investigate the quantification accuracy at varying activity concentration values. The activity concentrations at PET start time were 3.36, 1.96, 1.22, 0.73, 0.34, 0.20, 0.12, and 0.05 MBq/mL for the NEMA tumor phantom and 3.33, 1.97, 1.23, 0.73, 0.34, 0.20, 0.12, and 0.06 MBq/mL for the anthropomorphic tumor phantom.

PET acquisition

All phantom PET data were acquired using a single-bed position on a digital Biograph Vision 600 PET/CT scanner (Siemens Healthineers, Erlangen, Germany). Initially, the NEMA tumor phantom was scanned for 6 h and the resulting images were used to determine the recovery coefficients at high counting statistics. Thereafter, PET data of both phantoms were acquired for 30 min and used to reconstruct PET images using the total 30-min and 15-min acquisition time data. For attenuation correction, a low-dose CT scan was acquired (Care DOSE 4D, quality reference 160 mAs; CARE kV, quality reference 120 kV).

Image reconstruction

Images were reconstructed using three-dimensional ordinary Poisson ordered-subset expectation maximization (OSEM) with time-of-flight option (TOF) and with point-spread-function (PSF) modelling as previously recommended for quantitative ^{90}Y PET imaging on the Biograph Vision using 3 iterations and 5 subsets (*12*). Two post-reconstruction smoothing filter levels (all-pass and 5-mm Gaussian filter) were applied. The images had an almost cuboid-shaped voxel size with side lengths of 3.30x3.30x3.00 mm^3.

System spatial resolution measurements

The detailed description of the resolution phantom has been published by our group (*23*). Briefly, a cylindrical phantom (20 cm axial length, 20 cm outside diameter) contained line sources orthogonal to the transverse plane (or parallel to the PET system axis). The cavity of the phantom was filled with non-radioactive water. The line source, consisting of a refillable polyethylene tubing (0.5-mm inner diameter), was looped back through the phantom to provide four distances of 1 and 7 cm from the central axis of the scanner's field of view (FOV): (x = 1 cm, y = 0), (x = 7 cm, y = 0), (x = 0, y = 1 cm), (x = 0, y = 7 cm). The transverse spatial resolution was determined at four

positions each at the center (z = 0) and one-fourth of the scanner's FOV (z = ±1/4 FOV). The selected total activity in the line sources was 400–600 MBq.

The acquisition duration was 2 h and the resulting images were reconstructed using three-dimensional ordinary Poisson ordered-subset expectation maximization (OSEM) with TOF option and with PSF modelling as previously recommended for quantitative ^{90}Y PET imaging on the Biograph Vision using 3 iterations and 5 subsets (*12*). The images had an almost cuboid-shaped voxel size with side lengths of 0.83 x 0.83 x 3.00 mm^3. Two smoothing filter levels (all-pass and 5-mm Gaussian filter) were applied. The measured system spatial resolution (average full width at half maximum) was 3.3 mm for all-pass and 6.0 mm for a 5-mm Gaussian smoothing filter.

Patients

Patient characteristics

Retrospective analysis of clinical data was approved by the local Ethics Committee (permits no. 20-9558-BO). Data sets of three patients were included, who suffered from progressive, advanced-stage solitary fibrous tumor (SFT) and received a first cycle of ^{90}Y-FAPI-46 therapy under compassionate access following clinical indication. Radionuclide treatment was decided for in a multidisciplinary tumor board. All patients had either previously shown progressive disease during established treatment options or were not eligible for other established treatment concepts. The administered therapeutic activities were 8.90 GBq (patient#1), 3.82 GBq (patient#2), and 3.6 GBq (patient#3). Patient masses were 82 kg (patient#1), 51 kg (patient#2), and 51 kg (patient#3). Activities were determined using the 10-mL TEMA syringe geometry.

PET acquisition

PET/CT examinations were scheduled in reference to a previous study (*3*). PET data were acquired using two bed positions with 15 min acquisition time per bed position. Because of symptomatic patients and logistical reasons, serial PET/CT acquisition was performed at slightly

differing time points: 17, 22, 41 hours p.i. for patient #1, 2, 20, 43 hours p.i. for patient #2, and 1, 4, 20 hours p.i. for patient #3.

Image reconstruction

Images were reconstructed using the image reconstruction algorithm and the respective parameters (Poisson-OSEM PSF-TOF, iterations, voxel size) as described in the phantom section except for the smoothing level. For patient images, a 5-mm Gaussian smoothing filter was applied based on the phantom results. For attenuation correction, low-dose CTs were acquired (see above).

Phantom analysis

Mean recovery coefficients

NEMA tumor phantom PET data acquired for 6 hours were used to determine the mean RC values. The measured RC value (RC_{msd}) for each sphere was calculated by the ratio of the mean imaged activity concentration within the sphere boundary to the true activity concentration (using the dose calibrator-based value). A 3-parameter sigmoidal function was applied to fit the measured RC values as a function of the sphere diameter (d):

$$RC_{\mathrm{fit}} = a \cdot \left[1 + e^{-b \cdot (d - d_o)}\right]^{-1}$$

The symbols a, b, and d_0 are fitting parameters.

The estimated fitting parameters were a = 0.87, b = 0.35 mm^{-1}, d_0 = 9.34 mm for the non-filtered images and a = 0.81, b = 0.27 mm^{-1}, d_0 = 10.86 mm for the 5-mm Gaussian filtered images. Measured and fitted RC values for the different sphere size diameters of both tumor phantoms are listed in Supplemental Table S3.

Minimum detectable activity concentration

The images of the NEMA tumor phantom at varying activity concentration values were used to determine the minimum detectable activity concentration. Its determination has been previously described (*13*). In brief, first, the visual detectability of each sphere was determined in a human observer study (triple read). The detectability level was assessed using a three-point scale from "0" to "2". Spheres with a sum score of ≥3 were regarded as "detected" unless a single rating for a lesion was "0" (*24*). Second, the signal-to-noise ratio (*SNR*) of each sphere was determined:

$$ SNR = \frac{C_{\text{imaged}} - C_{\text{bgr}}}{\sigma_{\text{bgr}}} $$

The symbols C_{imaged}, C_{bgr}, and σ_{bgr} represent the mean sphere activity concentration, the background activity concentration, and the standard deviation of the phantom background, respectively. The background activity concentration was determined using 19 spherical VOIs with a diameter of 37.0 mm (corresponding to the diameter of the largest sphere of the phantom insert) placed at random positions. Third, visual detectability level and SNR were correlated in a histogram analysis to estimate the SNR threshold indicating detectability. Finally, the SNR was evaluated as a function of the activity concentration. Thereafter, the minimum detectable activity concentration was calculated for each sphere using the respective activity concentration at the threshold SNR.

Quantification accuracy evaluation

For a more realistic simulation of the scattering geometry of the human abdomen, the anthropomorphic abdominal tumor phantom was investigated. The anthropomorphic abdominal tumor phantom was applied to evaluate the activity concentration quantification accuracy as a function of activity concentration levels using the contour- and oversize-based approaches. To

evaluate the lesion quantification accuracy, the activity concentration ratios of PET-imaged to (decay corrected) dose calibrator-derived measurements were determined.

In the evaluation, a ±20% deviation range of the activity concentration ratio was regarded acceptable. This deviation range considered the overall maximum estimated uncertainty at 95%-confidence interval for (a) the ^{90}Y activity concentration measurement of ±7%, (b) a ^{18}F PET cross-calibration measurement of ±6% (*25*) and (c) the frequency of the positron-electron pair conversion of ±5% (*26-29*).

Minimum quantifiable activity concentration

The results of the quantification accuracy evaluations were used to estimate the minimum quantifiable activity concentration of reliability, that is, above that minimum quantifiable activity concentration the quantification appears to be reliable. In the derivation, the values of the quantification accuracy should lie within the ±20% deviation range.

Patient Analysis

In the patient analysis, key quantities related to the estimation of the tumor absorbed dose were derived. The procedure has previously been described (*3*). Briefly, the tumor volumes were estimated by manual segmentation (VOI technique) using the respective CT images and the VOIs were used to determine the tumor uptake values at three imaging time points. Mean tumor activity concentrations were determined using both the contour-based and the oversize-based approach. The resulting uptake curves were parameterized by fitting a mono-exponential function to the measured uptake values to determine the effective half-lives. The time-integrated activity coefficients (residence times) were determined and used to estimate the tumor absorbed doses using the sphere model of OLINDA/EXM (*30*).

Comparison of minimum detectable activity concentration between NEMA and anthropomorphic phantoms

For the anthropomorphic phantom, the human observer study revealed a SNR threshold of ≥7 to distinguish between "not-detected" and "detected" spheres. The minimum detectable activity concentration for each sphere size is shown in Supplemental Table S4. The 5-mm smoothed images provided an improved detectability for smaller spheres and the minimum detectable activity concentration was smaller by a mean factor of 0.54 compared to images without Gaussian smoothing. For a 30-min acquisition time, the minimum detectable activity concentration was reduced by a factor of 0.46 compared to the 15-min acquisition time.

In comparison to the NEMA phantom, the minimum detectable activity concentration values were mostly slightly higher, probably because of the differing scatter geometry and sphere positioning. The increase in minimum detectable activity concentration was more prominent for the smallest 10-mm sphere at the lower acquisition time of 15 min. We suggest that this is associated with the low absolute amount of ^{90}Y activity in this sphere resulting in poor counting statistics and with the proximity to the 40-mm sphere. Of note, this was also reflected in the investigation of the minimum quantifiable activity concentration of the anthropomorphic phantom (Table 2 in main text). In general, for the anthropomorphic phantom, the minimum detectable activity concentration values were in good agreement with the minimum quantifiable activity concentration values.

Supplemental Tables

Supplemental Table S1 – Activity concentration measurements of three independent geometries

Supplemental Table S1. Overview of the activity concentration measurements of three independent geometries and their respective dose calibrators to estimate the reference activity concentration of 3.58 MBq/mL along with its maximum error estimate of ±7% at the 95% confidence level – B&D activity measurements were considered as one independent measurement.

Geometry[a]	Dose calibrator (setting number)	Filling vol. (mL)	Activity (MBq)	Activity conc. (MBq/mL)	95%-Confidence Interval	Reference[b]
B&D	CRC-15R (52x10)	5.77	19.25	3.36[c]	10%	Siegel *et al.*
B&D	CRC-15R (56x10)	5.77	18.67	3.26[c]	10%	Zimmermann *et al.*
TEMA	CRC-25R (35x10)	7.82	30.04	3.84	3%	Eckert und Ziegler
TechneVial	CRC-15R (48x10)	9.69	34.81	3.59	7%	Vargas *et al.*

[a] 10-mL B&D syringe (Becton & Dickinson, Franklin Lakes, USA) with reference volume of 6 mL; 10-mL TEMA syringe with reference volume of 8 mL (Menny Medical, Mirandola, Italy); 11-mL TechneVial (Mallinckrodt, Staines-Upon-Thames, UK) with reference volume of 10 mL. [b] Siegel *et al.* J Nucl Med 2004,45:450; Zimmermann *et al.* Applied Radiation and Isotops 2004,60:511; calibration measurement performed by Eckert und Ziegler (Berlin, Deutschland); Vargas *et al.* EJNMMI Phys 2020,7:69. [c]As the two activity measurements with the two B&D geometries were considered as one independent measurement, average value of the B&D measurements (3.31 MBq/mL) was calculated first and further used in the determination of the mean activity concentration.

Supplemental Table S2 – Technical specifications for the Biograph Vision 600

Supplemental Table S2. Technical specifications for the Biograph Vision 600.

Detector material	LSO[a]
Detector element dimension (mm^3)	3.2x3.2x20
Detector elements per block	16x16
Total number of detector elements	60,800
Signal readout	SiPM[b] (2x2 per block)
Axial FOV (cm)	26.3
Transaxial FOV (cm)	78
Plane spacing (mm)	1.65
Image planes	119
Coincidence time window (ns)	4.7
Energy window (keV)	435–585
Energy resolution (%)	9
System time resolution (ps)	210
NEMA sensitivity (kcps/MBq)	16.4

[a] LSO, Lutetium oxyorthosilicate. [b] SiPM, silicon-photomultiplier.

Supplemental Table S3 – Measured and fitted recovery coefficients

Supplemental Table S2. Measured (RC_{msd}) and fitted (mean) recovery coefficient (RC_{fit}) of the sphere tumor phantoms for all-pass and 5-mm Gaussian smoothing.

| Phantom	Diameter (mm)	All-pass		5-mm smoothing	
		RC_{msd}	RC_{fit}	RC_{msd}	RC_{fit}
NEMA phantom					
	9.7	0.49	0.46	0.35	0.34
	12.6	0.66	0.66	0.52	0.50
	17.4	0.84	0.82	0.69	0.69
	22.2	0.85	0.86	0.76	0.77
	27.7	0.86	0.87	0.79	0.80
	37.0	0.88	0.87	0.83	0.81
	10.0	–	0.49	–	0.36
Anthropomorphic phantom					
	20.0	–	0.85	–	0.75
	30.0	–	0.87	–	0.81
	40.0	–	0.87	–	0.81

Supplemental Table S4 - Minimum detectable activity concentration for the anthropomorphic phantom

Supplemental Table S4. Estimated minimum detectable activity concentration (in MBq/mL) for the anthropomorphic phantom presenting results for the investigated sphere diameters, acquisition time durations (15 min vs. 30 min), and smoothing levels (all-pass vs. 5-mm Gaussian filter).

| Diameter (mm)	All-pass		5-mm smoothing	
	15 min	30 min	15 min	30 min
10	1.84	0.31	1.43	0.21
20	0.67	0.40	0.31	0.22
30	0.55	0.27	0.24	0.13
40	0.45	0.23	0.21	0.11

Supplemental Figures

Supplemental Figure S1
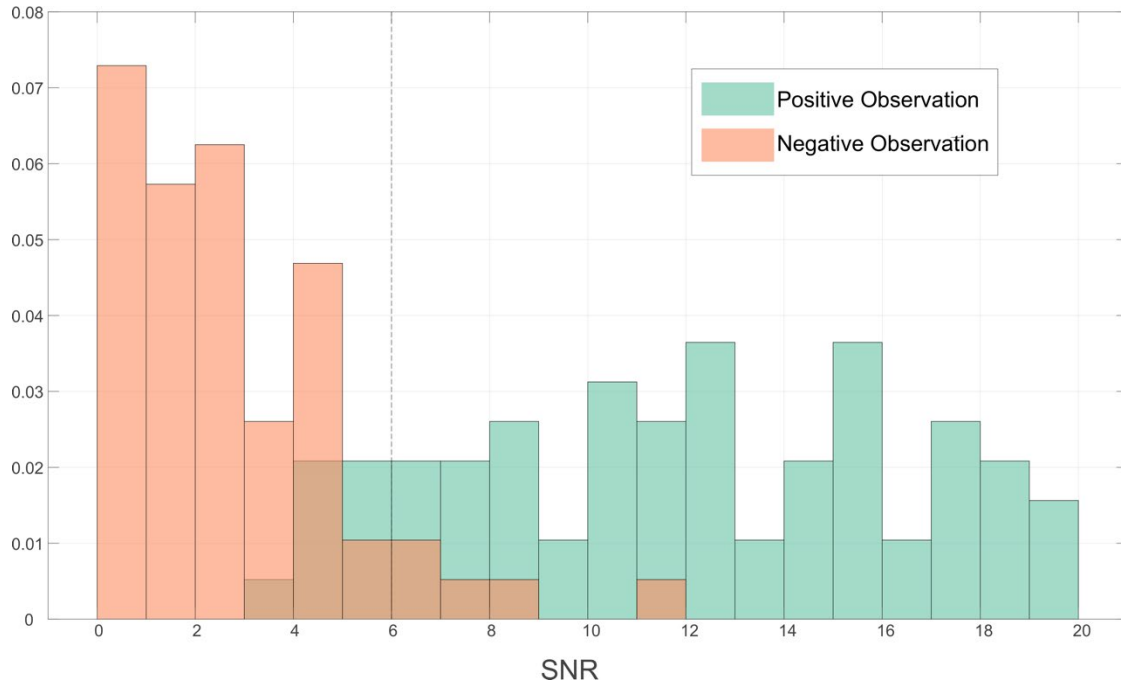
Supplemental Figure S1. Histogram analysis of the human observer study and sphere SNR derived from the NEMA tumor phantom. A threshold of SNR≥6 was determined to indicate detectability (dashed vertical line). For reasons of clarity, detected lesions with SNR larger or equal to 20 are not presented.

Supplemental Figure S2

A — 15 min PSF+TOF

B — 30 min PSF+TOF
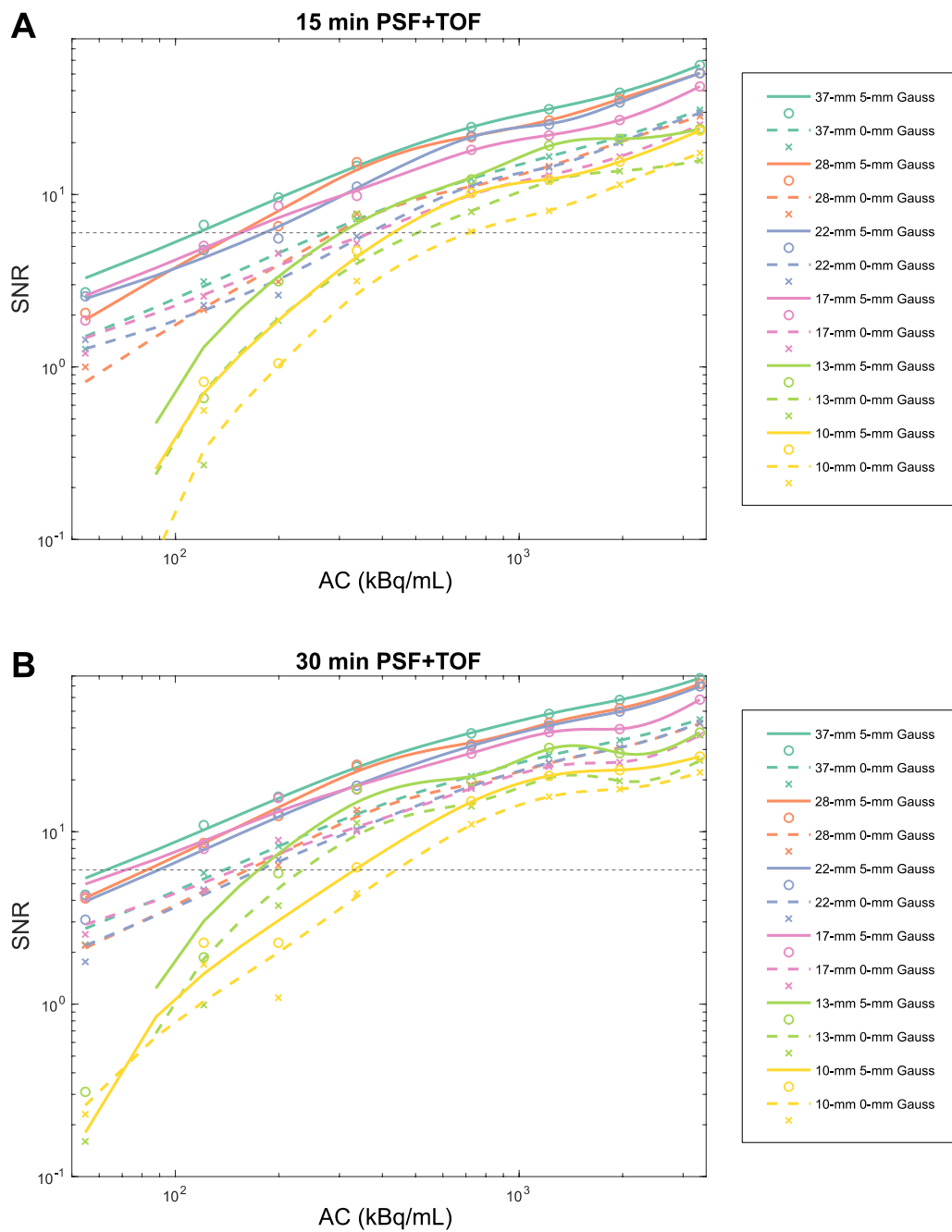
Supplemental Figure S2. SNR as a function of the activity concentration for an acquisition time of 15 min (A) and 30 min (B) derived from the NEMA tumor phantom. Dashed horizontal lines at SNR equals 6 indicate the threshold SNR to estimate the minimum detectable activity concentration.